



**HAL**  
open science

# Evaluation of atmospheric circulation of CMIP6 models for extreme temperature events using Latent Dirichlet Allocation

Nemo Malhomme, Bérengère Podvin, Davide Faranda, Lionel Mathelin

► **To cite this version:**

Nemo Malhomme, Bérengère Podvin, Davide Faranda, Lionel Mathelin. Evaluation of atmospheric circulation of CMIP6 models for extreme temperature events using Latent Dirichlet Allocation. 2024. hal-04484617

**HAL Id: hal-04484617**

**<https://cnrs.hal.science/hal-04484617>**

Preprint submitted on 29 Feb 2024

**HAL** is a multi-disciplinary open access archive for the deposit and dissemination of scientific research documents, whether they are published or not. The documents may come from teaching and research institutions in France or abroad, or from public or private research centers.

L'archive ouverte pluridisciplinaire **HAL**, est destinée au dépôt et à la diffusion de documents scientifiques de niveau recherche, publiés ou non, émanant des établissements d'enseignement et de recherche français ou étrangers, des laboratoires publics ou privés.

1       **Evaluation of atmospheric circulation of CMIP6 models for extreme**  
2       **temperature events using Latent Dirichlet Allocation**

3       Nemo Malhomme<sup>1,2</sup>, Bérengère Podvin<sup>3</sup>, Davide Faranda<sup>1</sup>, Lionel Mathelin<sup>2</sup>

4       <sup>1</sup> *ESTIMR, Université Paris-Saclay, CNRS, CEA, UVSQ, Laboratoire des sciences du climat et de*  
5       *l'environnement, 91191, Gif-sur-Yvette, France.*

6       <sup>2</sup> *LISN, CNRS, Université Paris-Saclay, 91405, Orsay, France.*

7       <sup>3</sup> *Université Paris-Saclay, CNRS, CentraleSupélec, Laboratoire EM2C, 91190, Gif-sur-Yvette,*  
8       *France.*

9       *Corresponding author:* Nemo Malhomme, nemo.malhomme@lsce.ipsl.fr

10 ABSTRACT: We study the ability of large-scale circulation models to reproduce extreme tem-  
11 perature events. To this end, we use a statistical clustering technique, Latent Dirichlet Allocation  
12 (LDA) to characterize sea-level pressure data over the north-Atlantic region. From the ERA5  
13 reanalysis dataset, the method extracts a basis of interpretable objects at synoptic scale, that we  
14 call “motifs”. Pressure data can be projected onto this basis, yielding motif weights that contain  
15 local information about the large-scale atmospheric circulation. We first examine how the weights  
16 statistics can be used to characterize extreme events in reanalysis data. We then compare the  
17 weights obtained from reanalysis data with those obtained from runs from four CMIP6 models.  
18 This allows us to quantify errors on each localized circulation pattern and identify model-agnostic  
19 and model-specific errors. On average, large-scale circulation is well predicted by all models, but  
20 model errors are increased for extreme events such as heatwaves and cold spells. A significant  
21 source of error was found to be associated with Mediterranean motifs for all models in all cases.  
22 Each model run can be characterized by a dynamic error associated with the global circulation  
23 pattern and a thermodynamic error associated with the predicted temperature. In the general case,  
24 this two-dimensional characterization is sufficient to discriminate between models. This remains  
25 possible in the cold spell case despite higher internal model variability, while all models perform  
26 similarly on heatwaves. The detailed characterization provided by LDA analysis is therefore well  
27 suited for model preselection for the study of extreme events.

## 28 **1. Introduction**

29 Heatwaves and cold spells both cause significant public health and safety risks (Weilhammer  
30 et al. (2021)), as well as infrastructure damage (Añel et al. (2017)). They are generally defined  
31 as temperature events significantly higher or below average over a period of at least several days.  
32 Studies have shown that both the number and the duration of heatwaves in the European region  
33 have increased by up to 15% since pre-industrial times (Frich et al. (2002), Alexander et al. (2006)).  
34 Examples of severe heatwaves include the European heatwave of 2003 (Fink et al. (2004)), or that  
35 of 2018 (McCarthy et al. (2019)). Both events have caused tens of thousands of deaths. While cold  
36 spell frequency and intensity have decreased since pre-industrial times (Seneviratne et al. (2021)),  
37 they still represent a hazard (López-Bueno et al. (2021)). For instance, we can cite the cold spell  
38 of 2017 over the Balkans (Anagnostopoulou et al. (2017)), which had consequent socio-economic  
39 impacts. In addition, when occurring during spring, cold spells can have a devastating impact  
40 on the development of plants and cause major losses of agricultural yields (Papagiannaki et al.  
41 (2014)). One such example is the cold spell of April 2021 described in Vautard et al. (2023b).

42 Heatwaves and cold spells produce anomalies reaching up to  $\pm 15^{\circ}\text{C}$  for several consecutive  
43 days. This implies that these events cannot be due to local thermodynamic drivers alone. They are  
44 explained in large part by changes in atmospheric circulation patterns (Rousi et al. (2022)), namely  
45 the ensemble of cyclones and anticyclones affecting a certain region at a given time. Cyclones  
46 and anticyclones advect warm or cold air from polar to tropical latitude and vice-versa through the  
47 mechanism of baroclinic instability (Wallace and Hobbs (2006)). With the temperature difference  
48 between pole and equator reaching up to 60 degrees, cyclones and anticyclones can advect warm  
49 and cold air and trigger heatwaves or cold spells. These cyclones and anticyclones evolve most  
50 of the time from west to east, because they are embedded in the jet stream. Sporadically, the jet  
51 stream creates large meanders that trap cyclones and anticyclones in the same position for several  
52 days (Krishnamurti (1961)). This phenomenon, called blocking, can cause persistence of warm  
53 or cold conditions in the same areas and trigger heatwave and cold spells (Faranda et al. (2016);  
54 Lupo (2021)). Conditions of atmospheric circulation patterns that can cause extreme temperature  
55 events are often referred to as their dynamic drivers (Chan et al. (2022)). Simulating the large  
56 excursions from the mean temperature responsible for hot and cold prolonged periods in Europe  
57 is crucial to understand, anticipate and mitigate the impacts of heatwaves and cold-spells. Global

58 and regional climate models are extensively used for this purpose both in present, past and future  
59 climate conditions (Eyring et al. (2016)).

60 However, models still face severe limitations in performing this task. According to the Coupled  
61 Model Intercomparison Project (CMIP, Meehl et al. (2000)), the statistical properties of extreme  
62 events are reasonably well captured by the models, but challenges persist in reproducing their  
63 frequencies and intensities, as well as in capturing local specificities (Kharin et al. (2013), Li  
64 et al. (2021)). For example, Vautard et al. (2023a) show that models underestimate the trend of  
65 evolution of heatwaves, and Jeong et al. (2021) show that models still underestimate the frequency  
66 of cold spells. Models are still unable to accurately reproduce the behavior of the atmosphere  
67 and ocean. In particular, they tend to underestimate the warming induced by climate change (van  
68 Oldenborgh et al. (2009)), and still contain inaccuracies that affect local circulation patterns (Scaife  
69 et al. (2010)), including those linked with extreme heat (D'Andrea et al.), and extreme cold (Davini  
70 and D'Andrea (2020)). Despite these biases compared to reality, models have made significant  
71 progress over the years. There have been increases in grid resolution, reaching a resolution as high  
72 as 1 km in regional models (Lucas-Picher et al. (2021)). Tuning techniques have been developed to  
73 reduce biases, such as regarding arctic sea ice cover extent, or the amplitude of Atlantic Meridional  
74 Overturning Circulation (Mignot et al. (2021)). Such improvements of the models have resulted in  
75 an increased ability to represent observed circulation patterns (Rodrigues et al. (2018)). To assess  
76 the advances and the remaining challenges, it is necessary to develop evaluation methodologies  
77 that give a comprehensive and accurate measure of a model's ability to capture extremes and their  
78 drivers.

79 Regarding dynamic drivers, it is difficult to study directly atmospheric patterns, owing to their  
80 high dimensionality. Several methods attempt to produce a reduced-order representation of the  
81 atmospheric circulation. One option is to categorize circulation fields into a set of weather  
82 regimes, large-scale quasi-stable states of atmospheric circulation (as first introduced in Rex  
83 (1950)). Regimes are effective to describe persistent weather patterns (such as in Vautard (1990)).  
84 This is useful to the study of extreme events, since some weather patterns, such as the above-  
85 mentioned blockings, can induce extreme events such as cold spells or heatwaves. However, by  
86 construction, weather regimes are not localized in space (Michelangeli et al. (1995)). They combine  
87 various atmospheric structures that are local, such as, for example, cyclones or anticyclones, into

88 large-scale atmospheric states. This loses the locality and the ability to differentiate between the  
89 components. They also typically exist at a time scale too large to define individual extreme events.  
90 Another technique is to use climate indices. Climate indices are one-dimensional variables that  
91 characterize the state of large-scale patterns, typically oscillations in oceanic circulation patterns  
92 that have a large influence over the global and regional climate (Stenseth et al. (2003)). They  
93 condense information into a parameter that can be directly studied, and its correlation with all  
94 kinds of observables and events measured (de Freitas and Grigorieva (2017)). This is especially  
95 useful to study oceanic oscillations, for example (Hanley et al. (2003)). However, since climate  
96 indices aggregate a lot of data in a single variable, relevant information about the underlying  
97 circulation can be missing.

98 In this study, we show that a technique introduced in Fery et al. (2022) can provide new insight on  
99 the atmospheric circulation of extreme weather events and give both local and global quantitative  
100 measures of the performance of climate models. The technique relies on a statistical learning tool  
101 known as Latent Dirichlet Allocation (LDA) (Blei et al. (2003)). Originally developed for text  
102 analysis, it has shown promise in capturing latent structures within complex datasets outside of  
103 natural language processing, such as in fluid mechanics (Frihat et al. (2021)), or environmental  
104 sciences (Valle et al. (2018)). In Fery et al. (2022), application of the LDA method to NCEP/NCAR  
105 sea-level pressure (SLP) maps led to the identification of latent variables, or “motifs”. Those motifs  
106 consist of synoptic objects, spatially localized pressure anomalies of the scale of 1000 km. Each  
107 map can be represented by a weighted combination of motifs. By monitoring the temporal evolution  
108 of the weights, they identified trends in impacts-defined extreme events.

109 In this paper, we show that LDA decomposition can be a useful tool to evaluate the performance  
110 of climate models, and in particular to quantify their ability to reproduce extreme temperature  
111 events. The paper is organized as follows. In section 2, we present the datasets to be analysed  
112 and our methods of analysis. In section 3, motifs extracted from the ERA5 SLP dataset are used  
113 to study the synoptic configuration of hot and cold temperature extremes occurring in France.  
114 A comparison between the reanalysis and climate models using this synoptic representation is  
115 reported in section 4. An evaluation of the climate models is carried out in section 5, based on  
116 the joint analysis of the synoptic representation error and the average temperature discrepancy. A  
117 conclusion is given in section 6.

## 118 2. Methods

### 119 a. Climate data

120 We choose the reanalysis dataset ERA5 (Hersbach et al. (2020)) as the ground truth to train  
121 LDA on and compare the models to. Our variable of study is the sea-level pressure (SLP), which  
122 contains the synoptic information relevant to a meteorological study, specifically the positions  
123 and extents of cyclones and anticyclones. An alternative for these properties would be 500 hPa  
124 geopotential height (z500). However, in ERA5 reanalysis data, z500 is computed from SLP rather  
125 than simulated directly. The data is converted into anomalies by removing the seasonal cycle,  
126 computed for each date as the average of all days corresponding to that date.

127 We chose to evaluate general circulation models, because they represent the physical detail of  
128 the atmospheric circulation. At time of writing, the CMIP6 project contains the state of the art  
129 in general circulation models. We select four CMIP6 models for which a high number of runs is  
130 available: IPSL-CM6A-LR (33 runs) (Boucher et al. (2020)), MIROC6 (50 runs) (Tatebe et al.  
131 (2019)), ACCESS-ESM1.5 (29 runs) (Ziehn et al. (2020)), and CanESM5 (25 runs) (Swart et al.  
132 (2019)).

### 133 b. Extreme event definition

134 Among extreme weather events, we study specifically cold spells and heatwaves. It is generally  
135 agreed upon that these terms refer to periods of temperatures significantly higher or below average  
136 for at least several days. However, any definition more precise is somewhat arbitrary, and there  
137 is no general consensus on a specific definition. A definition can be based on socio-economic  
138 impacts, on physical indicators, or the events can be automatically categorized through machine  
139 learning methods trained on data categorized by hand (such as in Liu et al. (2016)).

140 Since we are interested in evaluating model dynamics, while Fery et al. (2022) uses a definition  
141 based on impacts, we prefer to use a physics-based definition. In particular, we define a cold  
142 spell (resp. heatwave) as at least 3 consecutive days with average daily temperature below the  
143 0.03 quantile (resp. beyond the 0.97 quantile) of average temperatures over the studied period,  
144 from 1950 to 2021. Extreme events are defined for specific regions by considering the average  
145 temperatures over that region. To illustrate the method, we will consider cold spells and heatwaves

146 occurring in France. The results for five other countries, Italy, Spain, Poland, Germany and the  
147 UK, are available in supplemental material.

### 148 *c. Latent Dirichlet Allocation*

149 Latent Dirichlet Allocation (LDA) is an unsupervised statistical learning method originally  
150 devised in the field of natural language processing (Blei et al. (2003)). Its purpose is to extract,  
151 from a corpus of written documents, a set of latent variables called “topics” that describe their  
152 content. Documents are treated under the “bag of words” hypothesis, which assumes that the  
153 ordering of words in documents is irrelevant. A document is defined only by its counts of words  
154 belonging to a given vocabulary.

155 The number of topics  $K$  is a hyperparameter of the method, equivalent to a number of clusters.  
156 The topics are characterized by their distributions over the vocabulary. These are multinomial  
157 distributions parameterized by  $\beta$ , with components  $\beta_k, k \in [1, K]$  each defining the distribution  
158 associated to the topic of index  $k$ .

159 LDA is a soft clustering technique: each of the  $D$  documents in the corpus is associated with a  
160 distribution over the topics. This distribution, denoted  $c$ , is a multinomial distribution drawn from  
161 a Dirichlet distribution of parameter  $\alpha$ .

162 Given the parameters  $\alpha$  and  $\beta$ , LDA assumes that each document  $d$  of the corpus has been  
163 generated as follows:

- 164 • A total number of word positions  $N$  in the document  $d$  is drawn from a Poisson distribution.
- 165 • A topic composition  $c(d)$  is drawn for the document  $d$  (see Fig. 1) from a Dirichlet distribution  
166 of parameter  $\alpha$ .
- 167 • For each word position  $n$  in the document:
  - 168 – a topic index  $z_{d,n}$  is drawn from  $c(d)$ .
  - 169 – a word  $w_{d,n}$  is drawn from the word-topic distribution  $\beta_{z_{d,n}}$ .

170 The generative process is summarized in Fig. 2.



171 The joint distribution of all observable and hidden variables, knowing the parameters  $\alpha$  and  $\beta$ ,  
 172 is:

$$p((w_{d,n})_{d \in [1,D], n \in [1,N]} | \alpha, \beta) = \prod_{d=1}^D \int_c p(c(d) | \alpha) \prod_{n=1}^N \sum_{z_{d,n}=1}^K p(z_{d,n} | c(d)) p(w_{d,n} | z_{d,n}, \beta) dc(d) \quad (1)$$

173 with  $c(d)$  drawn from the Dirichlet distribution of parameter  $\alpha$ :

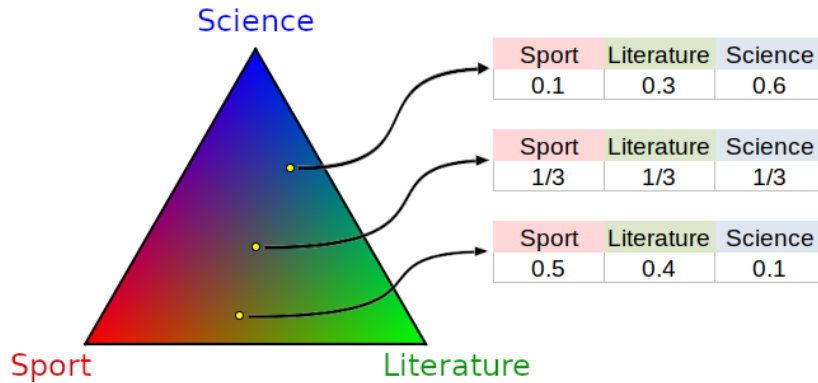
$$p(c(d) | \alpha) = \frac{1}{B(\alpha)} \prod_{k=1}^K c_k(d)^{\alpha_k - 1}, \quad B(\alpha) = \frac{\prod_{k=1}^K \Gamma(\alpha_k)}{\Gamma(\sum_{k=1}^K \alpha_k)} \quad (2)$$

174  $z_{d,n}$  drawn from the multinomial distribution  $c(d)$ :

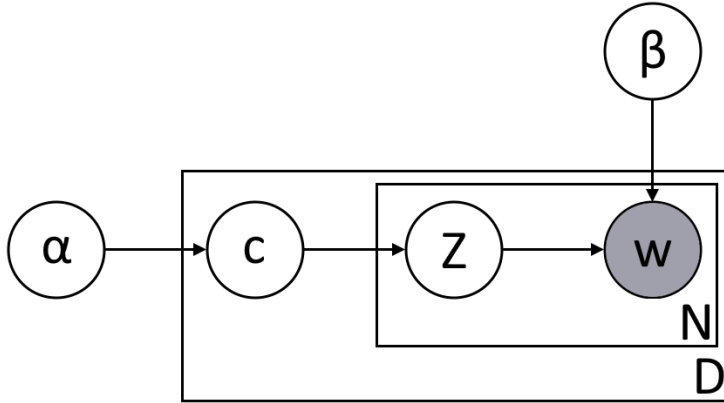
$$p(z_{d,n} = k | c(d)) = c_k(d) \quad (3)$$

175  $w_{d,n}$  drawn from the multinomial distribution  $\beta_z$ :

$$p(w_{d,n} = i | z_{d,n}, \beta) = \beta_{z_{d,n}, i} \quad (4)$$



176 FIG. 1. Example representation of the space of possible topic compositions, on which we define the Dirichlet  
 177 probability distribution parameterized by  $\alpha$ .



178 FIG. 2. Graphical model representation of the LDA generative process. Circles represent variables, greyed-out  
 179 circles being observed variables. Arrows represent the process of drawing a random variable from a distribution.  
 180 Rectangles represent reiteration of the process, with  $D$  being the number of documents, and  $N$  the number of  
 181 words in a document.

182 This method is applied to datasets of bidimensional climate variables maps where each spatial  
 183 map is reinterpreted as a document. Grid points, or cells, are reinterpreted as the words, with the  
 184 list of cells taking the role of the vocabulary. Field values at each cell are reinterpreted as word  
 185 counts. In this case, the cell-topics distributions  $\beta_k$  are defined over space and are called “motifs”.  
 186 Since the climate variable values are interpreted by LDA as word counts, they have to be digitized  
 187 and made non-negative. The real variable maps are therefore separated into two channels, one for  
 188 positive and one for negative values. This is equivalent to doubling the grid size over which the  
 189 maps are defined. The reader is referred for more details to Fery et al. (2022).

190 Analysis of a corpus of documents with LDA consists in examining the posterior distribution of  
 191 the topics  $\beta$ , topic proportions  $c$ , and topic assignments  $z$ . These are determined via a variational  
 192 Bayes approach aiming to maximize the evidence lower bound, which is related to the likelihood  
 193 of the observed data. An additional assumption of this approach is that the  $\beta_k$  are assumed to be  
 194 drawn from a Dirichlet prior of parameter  $\eta$ . The Dirichlet parameters  $\alpha$  and  $\eta$  respectively ensure  
 195 the sparsity of the document-topic and the topic-word distributions: there are generally few topics  
 196 in each document, and each topic is characterized by high occurrences of a few vocabulary words.

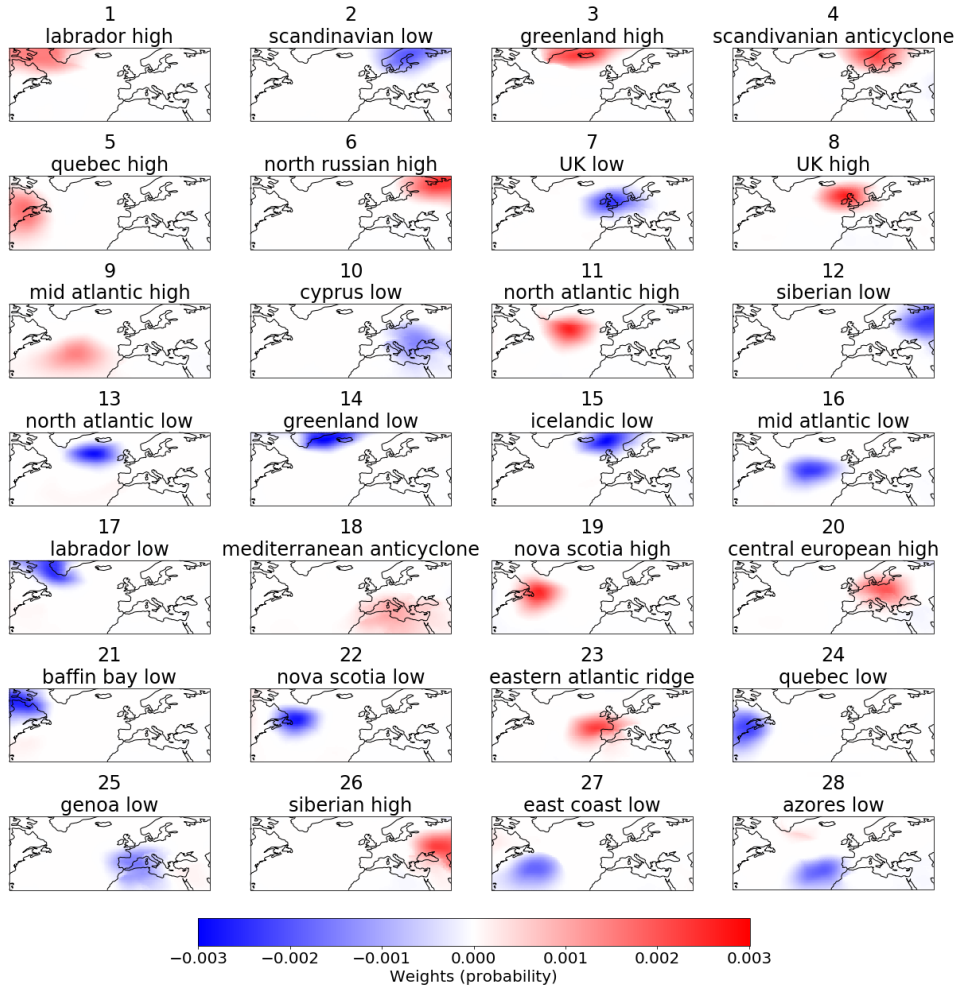
197 This sparsity property makes LDA particularly suited to provide models and decompositions that  
198 can be interpreted easily. For more information, see Hoffman et al. (2010).

199 For a given set of  $D$  maps, LDA returns motif distributions over grid cells  $(\beta_k)_{k \in [1, K]}$ , as well  
200 as the map compositions  $(c_k(d))_{d \in [1, D], k \in [1, K]}$ , where  $c_k(d)$  denotes the weight of motif  $k$  in map  
201  $d$ , such that  $\forall d \in [1, D], \sum_{k=1}^K c_k(d) = 1$ . The motif weights  $c(d)$  are always positive, unlike  
202 other decompositions such as Principal Component Analysis. The set of distributions  $(\beta_k)_{k \in [1, K]}$   
203 can be considered as a basis of motifs. Any map  $P$  defined on the grid (but not necessarily  
204 part of the original set) can be represented in this basis by its  $K$ -dimensional motif composition  
205  $c(P)$ . Different sets of maps can thus be compared efficiently through examination of their motif  
206 compositions. In practice, numerical implementation of LDA is carried out with the python module  
207 Gensim (Řehůřek and Sojka (2010)).

#### 208 *d. Application of LDA*

209 We apply LDA to ERA5 SLP data from the north-Atlantic region between  $22.5^\circ$  and  $70^\circ$  latitude  
210 and  $80^\circ$  and  $50^\circ$  longitude. Although higher resolutions are available, we used a spatial resolution  
211 of  $1^\circ$  as it was found to be sufficient to contain all relevant information about circulation patterns on  
212 the synoptic scale while maintaining manageable computation times. Our resolution is 48 points  
213 in latitude, 130 points in longitude, and we have two channels for positive and negative values.  
214 Therefore, the total number of values per map, noted  $N$ , is 12480. The temporal correlation time  
215 of synoptic circulation patterns is approximately 5 days. The full dataset (which will be referred to  
216 as general data) consists of daily averaged SLP anomaly fields from 1950 to 2021. The number of  
217 motifs was set to  $K = 28$ , as previous work (Fery et al. (2022)) showed, using a methodology from  
218 the field of dynamic systems (Faranda et al. (2017)), that this was the average local dimension of  
219 the SLP anomaly data.

223 These 28 motifs are shown in Fig. 3 and sorted by their average weights in decreasing order. To  
224 make discussion easier, names based on their signs and geographical locations were assigned to the  
225 motifs. Several motifs in the basis are approximate opposites of one another, such as Labrador high  
226 (1) and Labrador low (17), or Genoa low (25) and Mediterranean anticyclone (18). The resulting  
227 basis is similar to the one obtained in Fery et al. (2022), which was obtained for different reanalysis  
228 datasets at a lower resolution (NCEP/NCAR). Most of the motifs have recognizable equivalents



220 FIG. 3. The basis of 28 motifs learned by LDA from ERA5 SLP anomaly fields. Each motif is defined as a  
 221 probability distribution over space, with positive and negative channels. The names were given based on sign  
 222 and geographical location.

229 from one basis to the other, although some geographical locations may occasionally differ by a few  
 230 hundred kilometers. Motifs can be seen to be analogous to localized synoptic objects of a given  
 231 sign, such as cyclones and anticyclones. Therefore, motif weights in a SLP anomaly map directly  
 232 measure the contribution of the relevant synoptic objects.

233 LDA offers the possibility of reconstructing maps from a motif composition. The reconstruction  
 234 of map  $P$ , noted  $P^*$ , is obtained based on equation (5).

$$P^* = \|P\|_1 \sum_{k=1}^K c_k(P) \beta_k \quad (5)$$

235 where:

- 236 •  $\beta_k$  is the spatial distribution associated with motif  $k$ .
- 237 •  $c_k(P)$  is the weight of the  $k$ -th motif in the weight vector associated with the pressure map  
238  $P$ .
- 239 •  $\|P\|_1 = \sum_{i=1}^N |P_i|$  is the  $\ell_1$  norm of map  $P$  over all  $N$  grid cells. This term is a renormalization  
240 factor, allowing for direct comparison with physical fields.

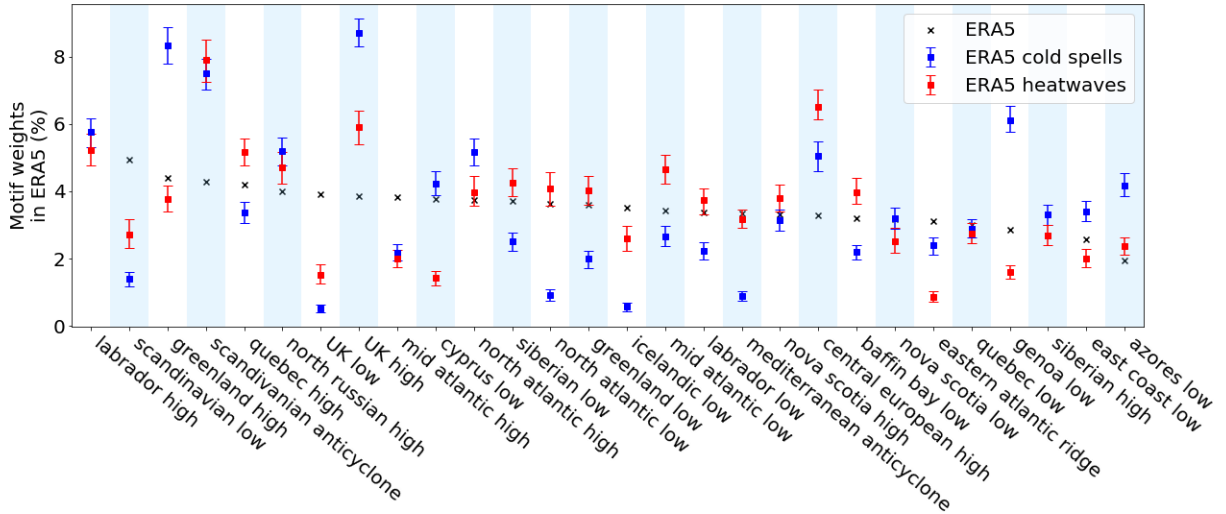
241 In this article, we reconstruct the average compositions of cold spells and heatwaves maps in a  
242 given model. In this case,  $c_k(P)$  is replaced with  $\langle\langle c_k(P) \rangle\rangle$ , where  $\langle\langle \cdot \rangle\rangle$  designates a conditional  
243 average over maps corresponding to the extreme event, and  $\|P\|_1$  is replaced with  $\|\langle\langle P \rangle\rangle\|_1$ .

### 244 3. Synoptic configuration of extreme events

245 We first use the decomposition into synoptic objects given by LDA to identify the atmospheric  
246 circulation patterns associated with cold spells and heatwaves. The patterns associated with extreme  
247 temperatures events in one country are expected to differ from those that would cause such events  
248 in another. As mentioned above, we focus our study on extreme temperature events occurring in  
249 France. The average synoptic configuration of reanalysis fields corresponding to cold spells (resp.  
250 heatwaves) is represented and compared to the average configuration of all reanalysis data in Fig.

251 4. Uncertainties are estimated by a resampling method called bootstrapping: many alternative  
252 sets of cold spell (resp. heatwave) days are generated by randomly sampling with replacements  
253 from the original cold spell (resp. heat wave) data. The average motif weights in these datasets  
254 are computed, and the 0.05 and 0.95 quantiles weights for each motif are used as lower and upper  
255 errors. We found that statistical convergence was reached with 500 datasets, with quantiles chosen  
256 to have a 90% confidence interval.

260 The synoptic configuration of extreme events is different from the average configuration of the  
261 general data. Cold spell circulation is dominated by northern anticyclones such as Greenland high,  
262 Scandinavian anticyclone and UK high, with more than 6% weights each. Correspondingly, the



257 FIG. 4. Average motif weight in the configuration of ERA5 SLP anomaly fields, in the general case (black), in  
 258 the case of cold spells in France (blue), and in the case of heatwaves in France (red). 90% confidence uncertainties  
 259 are determined by bootstrapping.

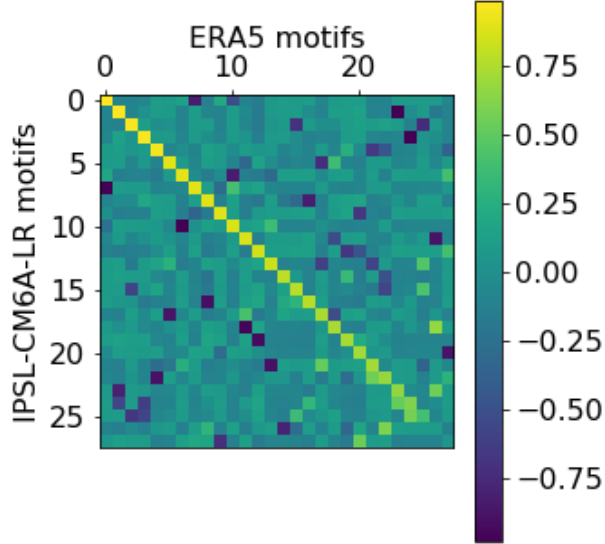
263 low pressure objects over those regions have less than half the weights they have in the general  
 264 data. Genoa low is also a key motif in French cold spells, being the fourth most represented  
 265 motif. Its opposite, the Mediterranean anticyclone, also has during cold spells half the weights  
 266 it has in general. Heatwave circulation is dominated by a smaller set of high-weights motifs,  
 267 mainly consisting of Scandinavian anticyclone, and central European high. The UK high is also  
 268 more prevalent during heatwaves than in general. Both types of extremes are associated with an  
 269 above-average weights of Scandinavian anticyclone and of UK high.

## 270 4. Evaluation of model representation

### 271 a. Robustness of the basis

272 We first establish that a unique basis can be used to compare models with reanalysis data. Fig. 5  
 273 shows the correlation matrix between the reanalysis data basis and that obtained from a run from a  
 274 IPSL-CM6A-LR model, which are respectively associated with cell-motif distributions  $\beta$  and  $\beta'$ .

275 The correlation matrix is obtained as follows: All fields are set to the same  $1^\circ$  resolution by linear  
 276 interpolation. For each matrix entry, the Pearson correlation coefficient  $\rho_{kl}$  between between motif  
 277



275 FIG. 5. Spatial correlation between the motifs of the bases obtained by applying LDA on ERA5 (vertical) and  
 276 on IPSL-CM6A-LR run 1 (horizontal). The order of the motifs has been adjusted to put the highest correlations  
 277 on the diagonal.

280  $k$  of basis  $\beta$  and motif  $l$  of basis  $\beta'$  is computed as shown in equation (6).

$$\rho_{kl} = \frac{\overline{(\beta_k - \bar{\beta}_k)} \overline{(\beta'_l - \bar{\beta}'_l)}}{\sqrt{\overline{(\beta_k - \bar{\beta}_k)^2}} \sqrt{\overline{(\beta'_l - \bar{\beta}'_l)^2}}} \quad (6)$$

281 where  $\bar{\cdot}$  designates the spatial average.

282 Motifs were reordered in order to give the same rank in the bases to the motifs with the highest  
 283 correlation. For the case considered, 22 out of 28 motifs have a clear equivalent in the other basis  
 284 with correlation of at least 0.7 (other choices of models gave similar results). Based on these  
 285 results, we consider that the motif basis learned from ERA5 is relevant to represent all model data.

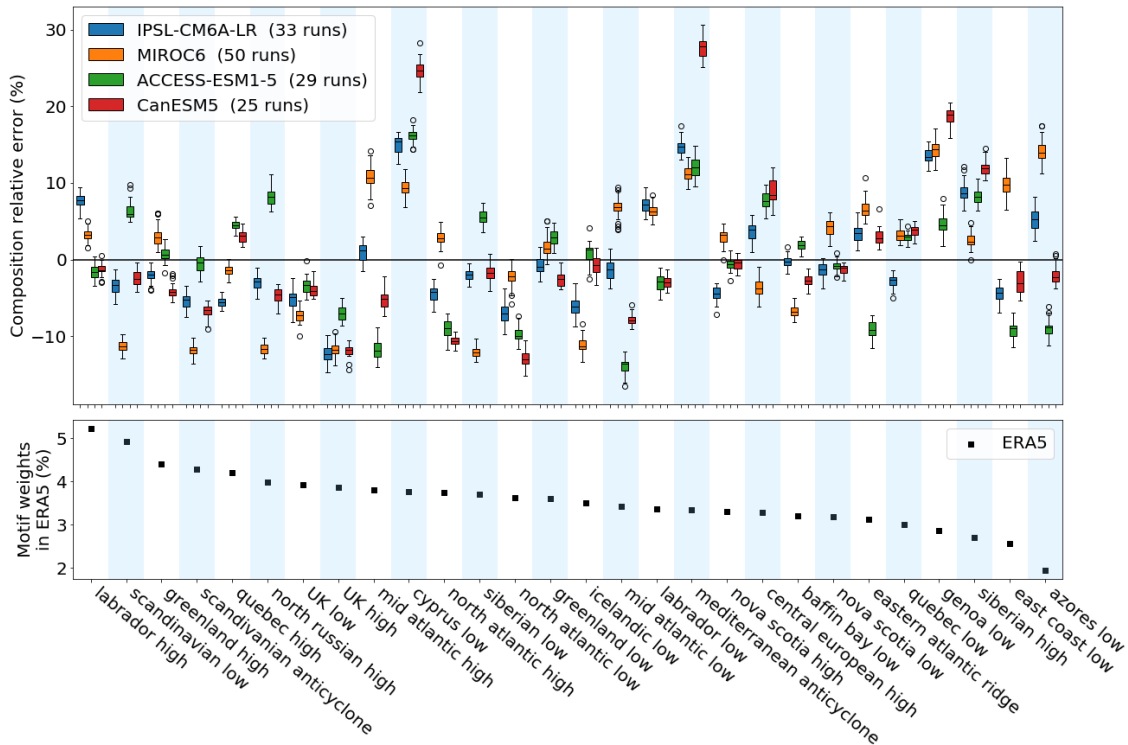
### 286 *b. General data case*

287 We project each run of the four models onto the motif basis learned from ERA5, then average  
 288 the resulting synoptic configuration of the fields over each run. We first consider all fields in the

289 datasets. For each run, the relative difference between the  $K$  motif weights in the model and that  
 290 in the reanalysis is computed following equation (7).

$$\forall k \in [1, K], E_k = \frac{\langle c_k(P^{m,r}) \rangle - \langle c_k(P) \rangle}{\langle c_k(P) \rangle} \quad (7)$$

291 where  $P$  corresponds to reanalysis maps,  $P^{m,r}$  corresponds to maps from run  $r$  of model  $m$ , and  
 292  $\langle \cdot \rangle$  designates the average over all maps in the dataset (model run or reanalysis). For each model,  
 293 the statistics of the error computed for each model run are shown in Figure 6, using box plots. The  
 294 mean weight of the motifs in the reanalysis data is also indicated for comparison.



295 FIG. 6. Top: Relative error on average motif weight between models and ERA5 reanalysis. The box edges  
 296 correspond to 1st and 3rd quartiles. The black line is the median. The whiskers extend to the furthest datapoint,  
 297 up to 1.5 times the difference between the 1st and 3rd quartiles. Datapoints beyond the whiskers are represented  
 298 as colorless circles. Bottom: average motif weight in the synoptic configuration of ERA5 fields.

299 The median relative errors, materialized by the black lines within the boxes, are relatively small.  
 300 In particular, the error is less than 15% for the eight most prevalent motifs in the reanalysis.  
 301 Overall, models represent well the reanalysis synoptic configuration. Relative errors made by



302 IPSL-CM6A-LR, MIROC6 and ACCESS-ESM1.5, which have resolutions of respectively  $38 \times 53$ ,  
303  $34 \times 92$ , and  $39 \times 69$  are all below 20%. We note that the largest error (25%) is observed for  
304 CanESM5, which has a resolution of  $17 \times 46$ . It is possible that these larger errors could be due to  
305 its coarser resolution. Moreover, the inner variability of the models (corresponding to the width of  
306 the boxes) is typically much smaller than the error (in 96 cases out of the 112 (87.5%), the model's  
307 internal variability is lower than its bias). This shows that all runs make similar predictions and  
308 also indicates the presence of a bias inherent to each model.

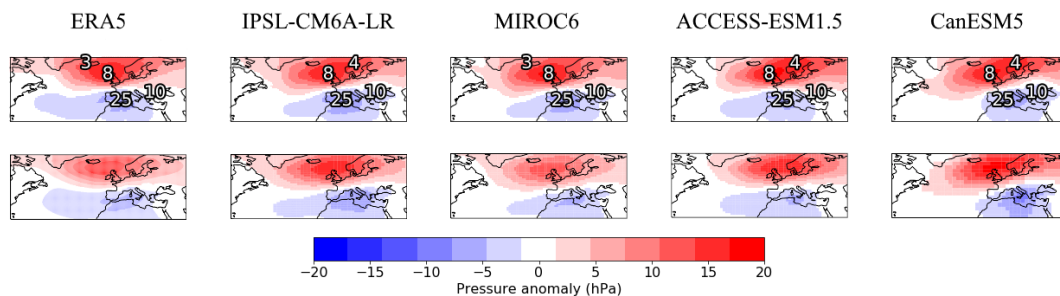
309 In addition, the motifs associated with the largest relative errors tend to be the same from one  
310 model to another. A multimodel ensemble mean would therefore not eliminate these biases.  
311 The largest errors are made on motifs located on the Mediterranean region. The Cyprus low  
312 and Mediterranean anticyclone motifs are over-represented in all runs of all four models. Every  
313 model run also over-represents Genoa low and under-represents UK high and low. Finally, the  
314 Scandinavian anticyclone is the fourth most prevalent motif in the reanalysis, with an average  
315 weight of more than 4% yet all models but ACCESS-ESM1.5 systematically under-represent it.  
316 These similarities in the model errors suggest that the origin of the errors could be common to all  
317 models.

### 318 *c. Model representation of cold spells*

319 We study how models capture the circulation patterns of extreme events. For this part, we focus  
320 on cold spells occurring in France. The datasets are filtered following the definition proposed in  
321 section 2.

322 The fields corresponding to the real and the reconstructed averages are represented in Fig. 7.  
323 The real average is obtained by taking a conditional average over all daily fields associated with  
324 a cold spell. The reconstructed average is obtained from the average motif compositions of the  
325 daily fields included in the conditional average, using equation (5). To identify the most significant  
326 motifs associated with each model, the two most prevalent cyclonic and the two most prevalent  
327 anticyclonic motifs in each case are annotated on the figure.

331 The overall synoptic structure associated with French cold spells consists of an anticyclonic  
332 structure in the north and a cyclonic structure in the south, with a corridor between the two  
333 slanted northeast-southwest, passing through the middle of France. For all models, the real average

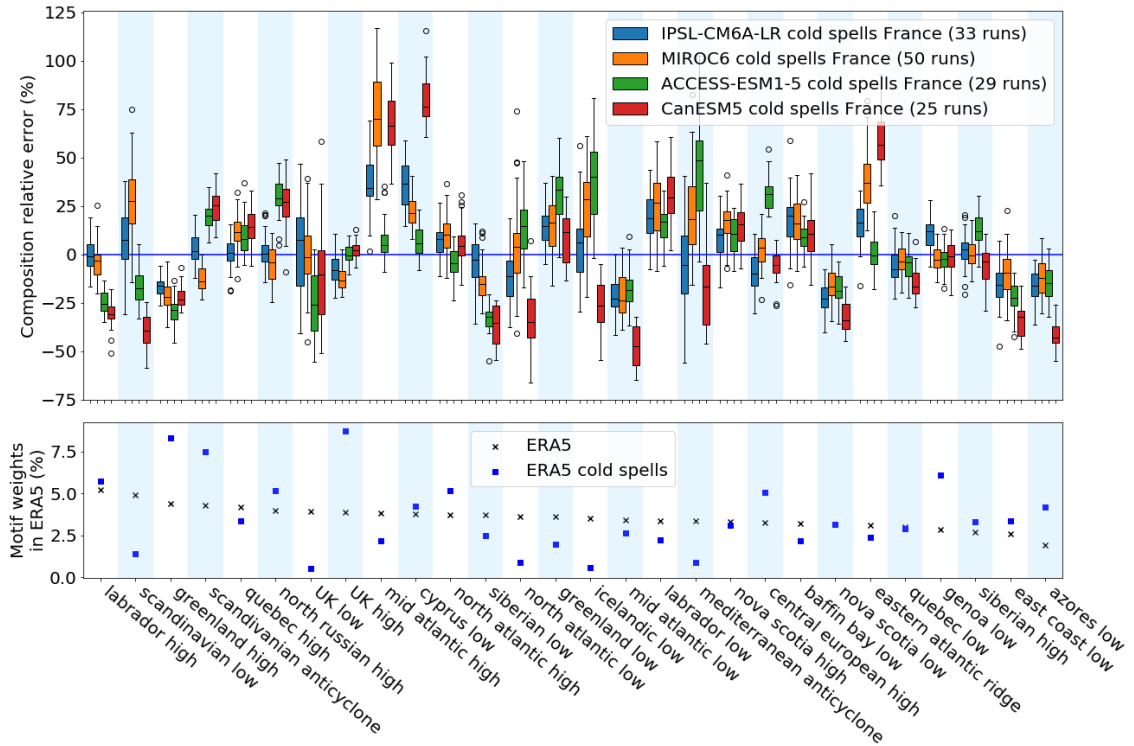


328 FIG. 7. Top line: Reconstruction of the average motif composition of cold spells in France according to  
 329 different models (columns). The two cyclones and the two anticyclones with highest average weights in each case  
 330 are annotated. Bottom line: Average SLP field for cold spells in France according to different models (columns).

334 is generally similar to its reconstructed average, which shows that LDA captures the synoptic  
 335 information contained in the real fields.

336 The model average fields are also in in good agreement with those of ERA5. They have the same  
 337 two most prevalent cyclones as ERA5, Cyprus low and Genoa low, and reproduce motif 8, UK  
 338 high, as a dominant motif. However some discrepancies are present: all models underestimate the  
 339 westward extent of the anticyclonic structure over the Atlantic. Only MIROC6 captures the fact  
 340 that Greenland high (motif 3) is more prevalent than Scandinavian anticyclone (motif 4), though as  
 341 seen in section 3, Greenland high and Scandinavian anticyclone are both relevant for French cold  
 342 spells (near 8% weights). In addition, on CanESM5, Genoa low is too intense, and the cyclonic  
 343 structure sees no extension to the west of the Mediterranean sea.

347 For a more detailed analysis, we show for each motif the relative errors in weights between the  
 348 reanalyses and the models in the case of cold spells occurring in France, in Fig. 8. The biases  
 349 are significantly higher for the cold extremes than for the general case. The variability among the  
 350 runs of each models is also higher than for the general case. The five most prevalent reanalysis  
 351 motifs during French cold spells are UK high, Greenland high, Scandinavian anticyclone, Genoa  
 352 low, Central European high. Most of these motifs are correctly represented by the models. The  
 353 significantly higher weights of UK high and Genoa low during cold spells are well captured by all  
 354 models with an error within the internal variability of all four models. Central European high is  
 355 also well represented by all models except by ACCESS-ESM1-5 which overestimates it by 25%.  
 356 The weight of Scandinavian anticyclone high is well captured by IPSL-CM6A-LR and MIROC6,



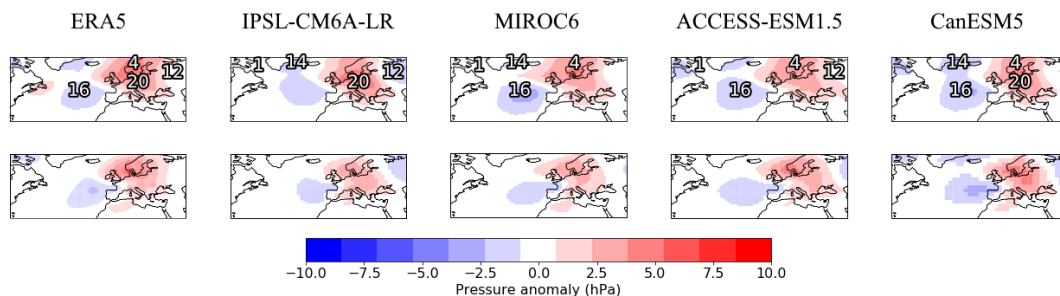
344 FIG. 8. Top: Relative error on average motif weight between models and ERA5 reanalysis in the case of cold  
 345 spells occurring in France. Bottom: average motif weight in the synoptic configuration of ERA5 fields, for cold  
 346 spells and in the general case.

357 while it is overestimated by 25% by the two other models. All models make about 25% error  
 358 on Greenland high. Higher errors are made on less relevant motifs where the reanalysis values  
 359 are lower. The most over-represented motifs are Cyprus low and Mid-Atlantic high for all models  
 360 except ACCESS-ESM1.5. We note that larger errors are generally observed for the lower resolution  
 361 model CAN-ESM5.

362 *d. Model representation of heatwaves*

363 We now focus on heatwaves occurring in France. We represent the real and reconstructed average  
 364 heatwave fields in Fig. 9, using the same methodology as in the previous section.

368 The SLP anomaly values are weaker than in the case of cold spells. This is because heatwaves are  
 369 more varied in configuration, leading to average error values closer to zero. There are differences  
 370 between the real and reconstructed fields. In ERA5 and all models, the anticyclonic structure over



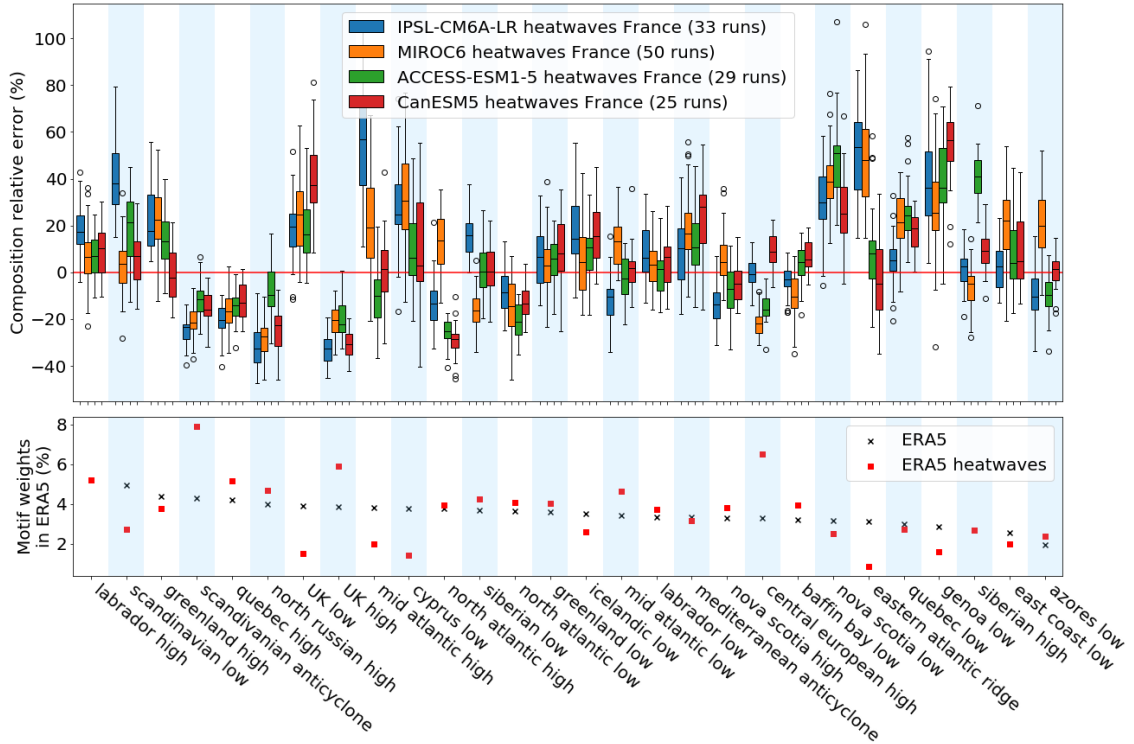
365 FIG. 9. Top line: Reconstruction of the average motif composition of heatwaves in France according to different  
 366 models (columns). The two cyclones and the two anticyclones with highest average weights in each case are  
 367 annotated. Bottom line: Average SLP field for heatwaves in France according to different models (columns).

371 Europe has a more crescent-like shape around the Atlantic cyclone, that changes into a arrow-like  
 372 shape in the LDA reconstruction. Still, the overall structure consisting of anticyclones over northern  
 373 and central Europe with a depression over the Atlantic is preserved by LDA reconstruction.

374 Models reproduce the overall structure of ERA5 circulation, with anticyclonic conditions on  
 375 northern and central Europe and cyclones over the Atlantic. Models disagree, with ERA5 and each  
 376 other, on the shape of those cyclones and the extent of the anticyclonic structure over northern  
 377 Atlantic. The most prevalent anticyclones in the reanalysis are the Scandinavian anticyclone (motif  
 378 4) and the Central European high (motif 20). Only CanESM5 reproduces this property. For the  
 379 other models, this leads to an anticyclonic structure that is weaker in the north for IPSL-CM6A-  
 380 LR, in the south for MIROC6, and less intense overall for ACCESS-ESM1.5. The most prevalent  
 381 cyclones are Siberian low (motif 12) and Mid-Atlantic low (motif 16). Only ACCESS-ESM1.5  
 382 reproduces this property.

383 For a more detailed analysis, we computed relative errors in motif weights between the reanalyses  
 384 and the models for heatwaves occurring in France. They are shown in Fig. 10.

388 In the case of heatwaves too, model biases and internal variabilities are higher than in the general  
 389 case. Which motifs are or are not relevant is generally well captured by the models. However,  
 390 the most relevant motifs tend to be underpredicted by the models. All models except ACCESS-  
 391 ESM1.5 under-represent by 20% on average the contribution of the most prevalent motif, which  
 392 is the Scandinavian anticyclone. The second most prevalent motif, the central European high,  
 393 is well represented by IPSL-CM6A-LR and CanESM5 but under-represented by about 20% by



385 FIG. 10. Top: Relative error on average motif weight between models and ERA5 reanalysis in the case of  
 386 heatwaves occurring in France. Bottom: average motif weight in the synoptic configuration of ERA5 fields, for  
 387 heatwaves and in the general case.

394 MIROC6 and ACCESS-ESM1.5. UK high, the third most prevalent motif, is under-represented  
 395 by 20% or more by almost all runs of all models. In general, motifs that have higher weights  
 396 than in the general case tend to be under-represented (as for instance Quebec high and north  
 397 Russian high), while motifs that have lower weights (UK low, Nova Scotia low, and Genoa low) are  
 398 over-represented. This shows that models underestimate the changes in atmospheric circulation  
 399 associated with heatwaves.

## 400 5. Global dynamic and thermodynamic error

### 401 a. General data case

402 LDA provides a decomposition of circulation patterns into motifs. Differences in motif weights  
 403 provide a quantitative measure of model predictive ability in terms of dynamics. The dynamic  
 404 error of run  $r$  of model  $m$ ,  $E_p^{m,r}$ , is computed according to equation (8).

$$E_P^{m,r} = \sum_{k=1}^K |\langle c_k(P^{m,r}) \rangle - \langle c_k(P) \rangle| \quad (8)$$

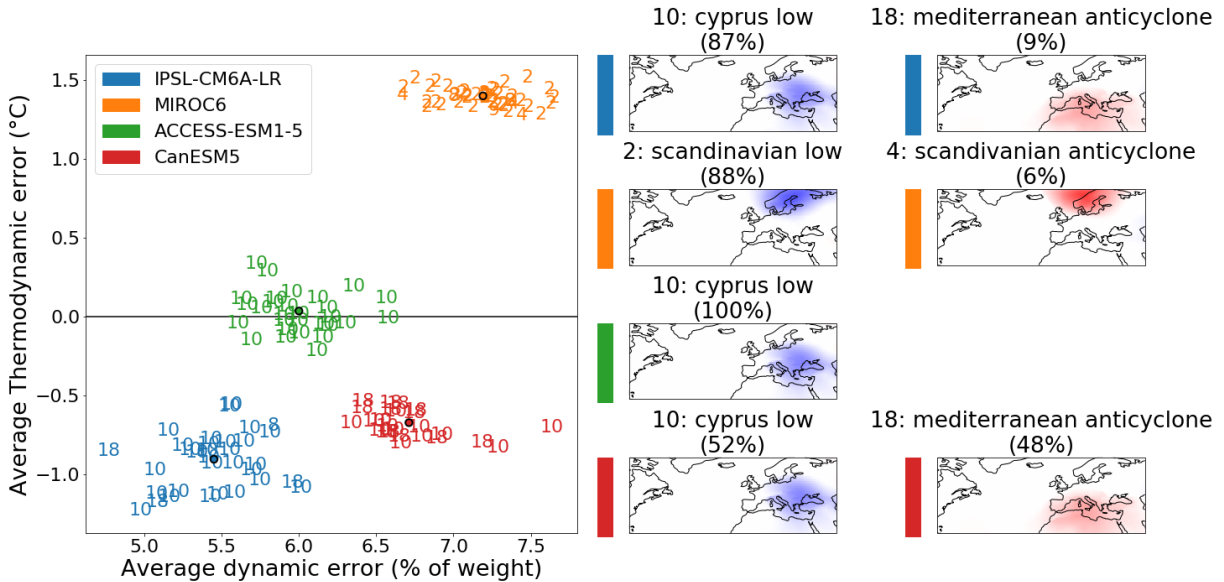
405 The dynamic error can be used to evaluate models comparatively, and produce rankings. An  
 406 important question is to determine whether evaluating models based on thermodynamic error, i.e.  
 407 the temperature difference between models and reanalysis data, would yield similar results. For  
 408 run  $r$  of model  $m$ , the thermodynamic error is computed as shown in equation (9), with  $T$  denoting  
 409 reanalysis temperature fields, and  $T^{m,r}$  those from run  $r$  of model  $m$ .

$$E_T^{m,r} = \langle \overline{T^{m,r}} \rangle - \langle \overline{T} \rangle \quad (9)$$

410 Each model run is represented as a point in the error plane  $(E_P^{m,r}, E_T^{m,r})$  shown in Fig. 11. In  
 411 addition, we annotate for each run the index of the motif which contributes the most to the dynamic  
 412 error. For each model, we show on the right of the figure the two motifs that appear most frequently  
 413 as the largest contributor to the error of a run (the proportion of runs each motif corresponds  
 414 to is indicated between parentheses) - except in the case of ACCESS-ESM1.5, where the largest  
 415 contributor is always Cyprus low.

420 Although some overlap between the models would be observed if only one kind of error was  
 421 considered, each model can be associated with a well-identified cluster in the 2-D error plane.  
 422 MIROC6 is the model with the highest dynamic and thermodynamic error, but with the lowest  
 423 thermodynamic variability. Unlike other models, it overpredicts the temperature. In contrast, the  
 424 IPSL-CM6A-LR model has the highest thermodynamic variability for a relatively low error (similar  
 425 to that of CanESM5), and it also corresponds to the lowest dynamic error. ACCESS-ESM1.5 has  
 426 the lowest thermodynamic error for a relatively low dynamic error.

427 As mentioned earlier, each run is annotated with the index of the motif contributing the most  
 428 to the dynamic error, which makes it possible to attribute the error to specific motifs and regions  
 429 in space. Cyprus low (motif 10) is the least well represented motif for all or almost all runs of  
 430 ACCESS-ESM1.5 and IPSL-CM6A-LR, as well as most runs of CanESM5. Another motif that is  
 431 occasionally the least well represented in runs of CanESM5 and IPSL-CM6A-LR is Mediterranean  
 432 anticyclone (motif 18), the opposite of Cyprus low. Both are eastern Mediterranean motifs.



416 FIG. 11. Run-average thermodynamic model error (average temperature difference with reanalysis), versus  
 417 run-average dynamic model error (average motif weights difference with reanalysis). The colored dots indicate  
 418 the average of all runs of a model. Each number corresponds to the motif contributing the most to the error in a  
 419 given run. The two most frequent such motifs for each model are displayed on the right.

433 We note that these motifs, which contribute the most to the error, are however not the most  
 434 prevalent motifs. The associated relative error is therefore necessarily large. This confirms that the  
 435 representation of the atmospheric circulation over the eastern Mediterranean region is a significant  
 436 issue for all models, particularly for models IPSL-CM6A-LR, ACCESS-ESM1.5, and CanESM5.  
 437 MIROC6 appears to differ from other models, as its error on the mean temperature is significantly  
 438 higher, and its dynamic error is attributed to different motifs than other models, the Scandinavian  
 439 low and Scandinavian anticyclone (motifs 2 and 4). This points to there being different sources of  
 440 error between MIROC6 and the other models.

441 *b. Model representation of extreme events*

442 We now consider extreme temperature events and compute the dynamic and thermodynamic  
 443 errors associated with heatwaves as well as cold spells. In that case, we eliminate the average bias,  
 444 so as to only look at the component specific to extreme events. We therefore define the anomalous  
 445 dynamic error  $E_{P,ex}^{m,r}$  similarly for heatwaves and cold spells following equation (10).

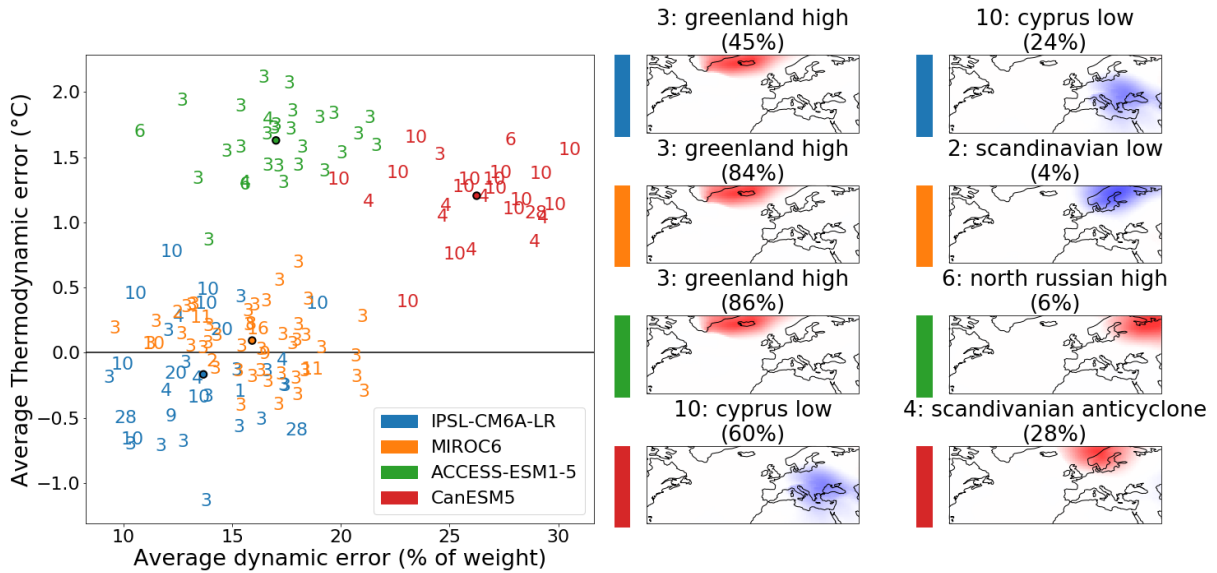
$$E_{P,ex}^{m,r} = \sum_{k=1}^K |\langle \langle c_k(P^{m,r}) \rangle \rangle - \langle \langle c_k(P) \rangle \rangle| - E_P^{m,r} \quad (10)$$

446 The anomalous thermodynamic error  $E_{T,ex}^{m,r}$  is defined for heatwaves and cold spells, for run  $r$  of  
 447 model  $m$  following equation (11).

$$E_{T,ex}^{m,r} = \langle \langle \overline{T^{m,r}} \rangle \rangle - \langle \langle \overline{T} \rangle \rangle - E_T^{m,r} \quad (11)$$

448 In subsequent figures, the dynamic and thermodynamic errors represented are only the anomalous  
 449 errors defined above. The average errors studied in Fig. 11 are eliminated. However, we note that  
 450 the general conclusions reported below did not change when these errors were taken into account.

457 Fig 12 shows model anomalous thermodynamic error against model anomalous dynamic error  
 in the case of cold spells occurring in France.



451 FIG. 12. Run-average thermodynamic model error (average temperature difference with reanalysis) on cold  
 452 spells in France, versus run-average dynamic model error (average motif weights difference with reanalysis) on  
 453 same extremes. We eliminate the errors computed in the general case, so as to look only at errors specific to  
 454 extreme events. The colored dots indicate the average of all runs of a model. Each number corresponds to the  
 455 motif contributing the most to the error in a given run. The two most frequent such motifs for each model are  
 456 displayed on the right.

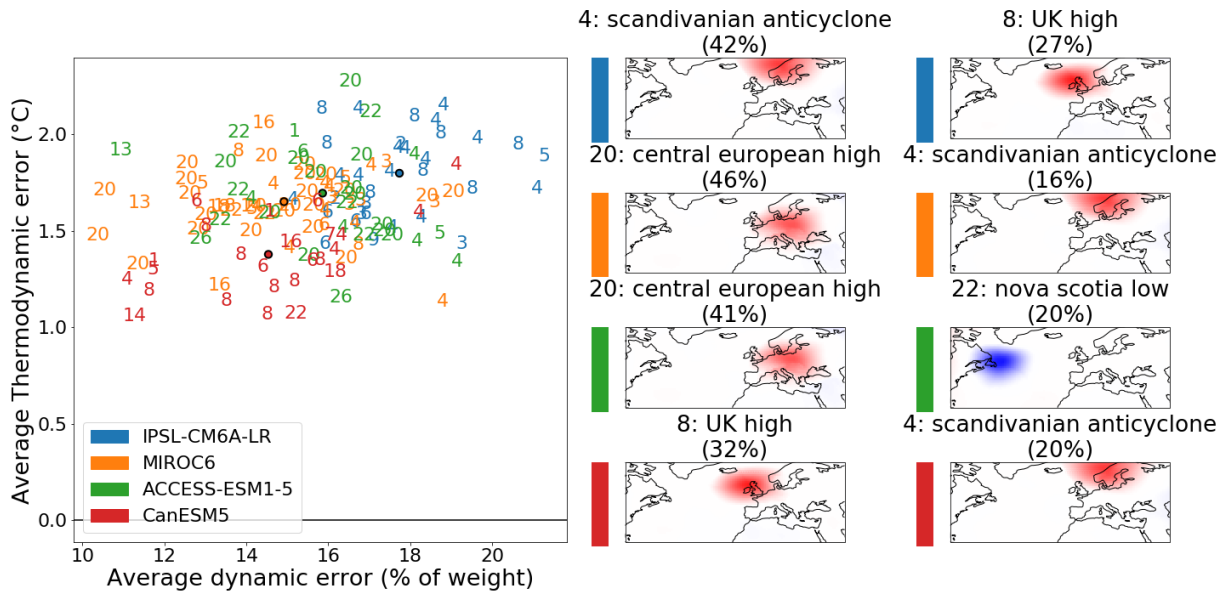


458 Inner model variability is higher in the cold extreme case than in the full dataset case, both for  
459 dynamic and thermodynamic error. There are three distinct clusters in error space, the differences  
460 between them being bigger than internal model variabilities. The first cluster corresponds to model  
461 CanESM5. It is the model with the highest dynamic error, and has a high thermodynamic error.  
462 The second cluster corresponds to model ACCESS-ESM1.5. ACCESS-ESM1.5 has the highest  
463 thermodynamic error, underpredicting the lowering of temperature due to cold spells by more than  
464 1.5°C on average. Its dynamic error is comparable to that of MIROC6, and both are made in  
465 majority on the same motif (Greenland high). The third cluster consists of two models, IPSL-  
466 CM6A-LR and MIROC6. With the general bias removed, the temperature value from reanalysis  
467 is within the internal variability of both these models. They are also associated with the lowest  
468 dynamic error. This cluster appears to be closest to reanalysis. On average, IPSL-CM6A-LR has  
469 a slightly lower dynamic error than MIROC6, but the difference is lower than internal variability.

470 Greenland high (motif 3) is the least well represented motif on more than 80% of MIROC6 and  
471 ACCESS-ESM1.5 runs, as well as 45% of ISPL-CM6A-LR runs. However this does not signify  
472 a major model error in the local atmospheric circulation, as the relative error is small, and the  
473 significant contribution simply reflects the predominance of the motif in the composition of cold  
474 spells. In contrast, for a majority of CanESM5 runs, as well as 24% of IPSL-CM6A-LR runs, the  
475 largest contribution to the dynamic error is due to Cyprus low (motif 10). It is not a particularly  
476 dominant motif, but one on which the model makes a significant relative error (75% on median,  
477 see Fig. 8). Again this suggests a major flaw in the model representation of local circulation over  
478 the Mediterranean.

485 In Fig. 13 we plot model anomalous thermodynamic error against model anomalous dynamic  
486 error in the case of heatwaves occurring in France. The inner variability of the models for heatwaves  
487 is similar to the cold spell case. However, both thermodynamic and dynamic biases associated  
488 with the models are closer, so that in the 2-D error space, regions occupied by each model are  
489 overlapping. All four models are associated with similar thermodynamic errors, between +1.0 and  
490 +2.5°C - as these biases are all positive, they cannot be removed by use of a multimodel mean.

491 Still, some differences can be made between the models. CanESM5 has the lowest of both types  
492 of error on average and IPSL-CM6A-LR the highest, but the differences are lower than model



479 FIG. 13. Run-average thermodynamic model error (average temperature difference with reanalysis) on heat-  
 480 waves in France, versus run-average dynamic model error (average motif weights difference with reanalysis)  
 481 on same extremes. We eliminate the errors computed in the general case, so as to look only at errors specific  
 482 to extreme events. The colored dots indicate the run-average value. Each number corresponds to the motif  
 483 contributing the most to the error in a given run. The two most frequent such motifs for each model are displayed  
 484 on the right.

493 internal variabilities. In addition, motifs that contribute the most to the error vary significantly  
 494 more from run to run than for both general data and cold spells. In particular, no motif dominates  
 495 the error in a majority of runs of any model, although some appear more often than others. Central  
 496 European high (motif 20) appears most frequently as the most significant contributor to the error  
 497 in runs of both MIROC6 and ACCESS-ESM1.5, while Scandinavian anticyclone (motif 4) makes  
 498 the largest error contributions in multiple runs of IPSL-CM6A-LR, MIROC6 and CanESM5.  
 499 However, we note that both Central European high and Scandinavian anticyclone are dominant  
 500 motifs in heatwaves, so their presence does not reflect a significant relative motif error in the  
 501 models. To sum up, all models appear to perform comparably for the representation of heat waves,  
 502 and it seems difficult to identify specific error characteristics in the models.

## 503 **6. Conclusion**

504 In this paper, we use a statistical learning method called Latent Dirichlet Allocation (LDA) to  
505 study the circulation dynamics of ERA5 reanalysis data and CMIP6 general circulation models.  
506 Applied to sea-level pressure fields of the north-Atlantic region from ERA5 data, LDA yields a set  
507 of latent variables called “motifs” that are recognizable localized synoptic-scale meteorological  
508 objects, such as cyclones and anticyclones. By projecting daily sea-level pressure data onto this  
509 basis, we obtain the motif composition, which provides a sparse, low-dimensional representation of  
510 atmospheric circulation that can be physically interpreted as the associated synoptic configuration.  
511 We showed that synoptic configurations averaged over cold spells and heatwaves were both different  
512 from each other and from the average taken over the full data.

513 Using this reanalysis motif basis, we computed the synoptic configuration of runs from 4 different  
514 CMIP6 models. Evaluation of the models was based on comparing the statistics of model synoptic  
515 configurations with that of reanalysis ones. Differences between models and reanalysis could  
516 then be directly attributed to changes in the average weights of individual motifs. This local  
517 characterization of the circulation could help discriminate between model predictions, and also  
518 help identify the origin of model limitations. Generally speaking, a good agreement was found for  
519 general data, while discrepancies were larger for extreme events. In all cases, the largest source  
520 of model error was due to the circulation over the eastern Mediterranean region. Moreover, all  
521 models tended to underestimate the changes in atmospheric circulation associated with heat waves.

522 A global dynamic error, based on synoptic configuration differences with reanalysis, was com-  
523 pared with a thermodynamic error, based on the differences in average temperature. These two  
524 indicators were found to be sufficient to help discriminate between models when considering gen-  
525 eral data. Discriminating between models was still possible in the cold spell case, while models  
526 performed comparably on heatwaves. This method could therefore be used to determine whether  
527 specific models are best suited to the study of a given type of event. Characterization of the error  
528 is also relevant to knowing how to aggregate model data, and identifying the biases that can be  
529 eliminated this way.

## 530 **7. Acknowledgements**

531 This work is supported by CNRS-MITI (80 PRIME project ACLIM). We thank Robin Noyelle,  
532 Camille Cadiou and Mireia Ginesta-Fernandez for their help in processing the data.

## 533 **8. Availability statement**

534 This work makes use of the Gensim python module, which is publicly available for download  
535 through the pip interface. ERA5 reanalysis data are made publicly available by the Copernicus  
536 program, see <https://doi.org/10.24381/cds.143582cf>. Model datasets used in this article are sim-  
537 ulations from the CMIP6 project for the “historical” experiment, by the models IPSL-CM6A-LR,  
538 MIROC6, ACCESS-ESM1.5 and CMIP6. The data is publicly available thanks to the World  
539 Climate Research Programme, and can be found at: <https://esgf-node.llnl.gov/search/cmip6>.

540 **9. References**

541 **References**

- 542 L. V. Alexander, X. Zhang, T. C. Peterson, J. Caesar, B. Gleason, A. M. G. Klein Tank,  
543 M. Haylock, D. Collins, B. Trewin, F. Rahimzadeh, A. Tagipour, K. Rupa Kumar, J. Re-  
544 vadekar, G. Griffiths, L. Vincent, D. B. Stephenson, J. Burn, E. Aguilar, M. Brunet, M. Tay-  
545 lor, M. New, P. Zhai, M. Rusticucci, and J. L. Vazquez-Aguirre. Global observed changes  
546 in daily climate extremes of temperature and precipitation. *Journal of Geophysical Re-*  
547 *search: Atmospheres*, 111(D5), 2006. ISSN 2156-2202. doi: 10.1029/2005JD006290.  
548 URL <https://onlinelibrary.wiley.com/doi/abs/10.1029/2005JD006290>. \_eprint:  
549 <https://onlinelibrary.wiley.com/doi/pdf/10.1029/2005JD006290>.
- 550 C. Anagnostopoulou, K. Tolika, G. Lazoglou, and P. Maheras. The Exceptionally Cold January of  
551 2017 over the Balkan Peninsula: A Climatological and Synoptic Analysis. *Atmosphere*, 8(12):  
552 252, Dec. 2017. ISSN 2073-4433. doi: 10.3390/atmos8120252. URL <https://www.mdpi.com/2073-4433/8/12/252>. Number: 12 Publisher: Multidisciplinary Digital Publishing  
553 Institute.  
554
- 555 J. A. Añel, M. Fernández-González, X. Labandeira, X. López-Otero, and L. De la Torre. Impact  
556 of Cold Waves and Heat Waves on the Energy Production Sector. *Atmosphere*, 8(11):209,  
557 Nov. 2017. ISSN 2073-4433. doi: 10.3390/atmos8110209. URL <https://www.mdpi.com/2073-4433/8/11/209>. Number: 11 Publisher: Multidisciplinary Digital Publishing Institute.  
558
- 559 D. M. Blei, A. Y. Ng, and M. I. Jordan. Latent dirichlet allocation. *The Journal of Machine*  
560 *Learning Research*, 3(null):993–1022, Mar. 2003. ISSN 1532-4435.
- 561 O. Boucher, J. Servonnat, A. L. Albright, O. Aumont, Y. Balkanski, V. Bastrikov, S. Bekki, R. Bon-  
562 net, S. Bony, L. Bopp, P. Braconnot, P. Brockmann, P. Cadule, A. Caubel, F. Cheruy, F. Codron,  
563 A. Cozic, D. Cugnet, F. D’Andrea, P. Davini, C. de Lavergne, S. Denvil, J. Deshayes, M. Dev-  
564 illiers, A. Ducharne, J.-L. Dufresne, E. Dupont, C. Éthé, L. Fairhead, L. Falletti, S. Flavoni,  
565 M.-A. Foujols, S. Gardoll, G. Gastineau, J. Ghattas, J.-Y. Grandpeix, B. Guenet, E. Guez, Li-  
566 onel, E. Guilyardi, M. Guimberteau, D. Hauglustaine, F. Hourdin, A. Idelkadi, S. Joussaume,  
567 M. Kageyama, M. Khodri, G. Krinner, N. Lebas, G. Levvasseur, C. Lévy, L. Li, F. Lott,

568 T. Lurton, S. Luysaert, G. Madec, J.-B. Madeleine, F. Maignan, M. Marchand, O. Marti,  
569 L. Mellul, Y. Meurdesoif, J. Mignot, I. Musat, C. Ottlé, P. Peylin, Y. Planton, J. Polcher,  
570 C. Rio, N. Rochetin, C. Rousset, P. Sepulchre, A. Sima, D. Swingedouw, R. Thiéblemont,  
571 A. K. Traore, M. Vancoppenolle, J. Vial, J. Vialard, N. Viovy, and N. Vuichard. Presenta-  
572 tion and Evaluation of the IPSL-CM6A-LR Climate Model. *Journal of Advances in Modeling*  
573 *Earth Systems*, 12(7):e2019MS002010, 2020. ISSN 1942-2466. doi: 10.1029/2019MS002010.  
574 URL <https://onlinelibrary.wiley.com/doi/abs/10.1029/2019MS002010>. \_eprint:  
575 <https://onlinelibrary.wiley.com/doi/pdf/10.1029/2019MS002010>.

576 P. W. Chan, J. L. Catto, and M. Collins. Heatwave–blocking relation change likely dominates over  
577 decrease in blocking frequency under global warming. *npj Climate and Atmospheric Science*, 5  
578 (1):68, 2022.

579 P. Davini and F. D’Andrea. From CMIP3 to CMIP6: Northern Hemisphere Atmospheric Block-  
580 ing Simulation in Present and Future Climate. *Journal of Climate*, 33(23):10021–10038,  
581 Dec. 2020. ISSN 0894-8755, 1520-0442. doi: 10.1175/JCLI-D-19-0862.1. URL <https://journals.ametsoc.org/view/journals/clim/33/23/jclid190862.xml>. Publisher:  
582 American Meteorological Society Section: Journal of Climate.

584 C. R. de Freitas and E. A. Grigorieva. A comparison and appraisal of a comprehensive range  
585 of human thermal climate indices. *International Journal of Biometeorology*, 61(3):487–512,  
586 Mar. 2017. ISSN 1432-1254. doi: 10.1007/s00484-016-1228-6. URL [https://doi.org/10.](https://doi.org/10.1007/s00484-016-1228-6)  
587 [1007/s00484-016-1228-6](https://doi.org/10.1007/s00484-016-1228-6).

588 F. D’Andrea, J.-P. Duvel, G. Rivière, R. Vautard, J. Cattiaux, D. Coumou, D. Faranda, T. Happé,  
589 A. Ribes, and P. Yiou. Summer Deep Depressions Increase Over the North Atlantic.

590 V. Eyring, S. Bony, G. A. Meehl, C. A. Senior, B. Stevens, R. J. Stouffer, and K. E. Taylor.  
591 Overview of the Coupled Model Intercomparison Project Phase 6 (CMIP6) experimental design  
592 and organization. *Geoscientific Model Development*, 9(5):1937–1958, May 2016. ISSN 1991-  
593 959X. doi: 10.5194/gmd-9-1937-2016. URL [https://gmd.copernicus.org/articles/  
594 9/1937/2016/gmd-9-1937-2016.html](https://gmd.copernicus.org/articles/9/1937/2016/gmd-9-1937-2016.html). Publisher: Copernicus GmbH.

- 595 D. Faranda, G. Masato, N. Moloney, Y. Sato, F. Daviaud, B. Dubrulle, and P. Yiou. The switching  
596 between zonal and blocked mid-latitude atmospheric circulation: a dynamical system perspec-  
597 tive. *Climate Dynamics*, 47:1587–1599, 2016.
- 598 D. Faranda, G. Messori, and P. Yiou. Dynamical proxies of North Atlantic predictability and  
599 extremes. *Scientific Reports*, 7(1):41278, Jan. 2017. ISSN 2045-2322. doi: 10.1038/srep41278.  
600 URL <https://www.nature.com/articles/srep41278>. Number: 1 Publisher: Nature Pub-  
601 lishing Group.
- 602 L. Fery, B. Dubrulle, B. Podvin, F. Pons, and D. Faranda. Learning a Weather Dictio-  
603 nary of Atmospheric Patterns Using Latent Dirichlet Allocation. *Geophysical Research*  
604 *Letters*, 49(9):e2021GL096184, 2022. ISSN 1944-8007. doi: 10.1029/2021GL096184.  
605 URL <https://onlinelibrary.wiley.com/doi/abs/10.1029/2021GL096184>. \_eprint:  
606 <https://onlinelibrary.wiley.com/doi/pdf/10.1029/2021GL096184>.
- 607 A. H. Fink, T. Brücher, A. Krüger, G. C. Leckebusch, J. G. Pinto, and U. Ulbrich. The 2003  
608 European summer heatwaves and drought - synoptic diagnosis and impacts. *Weather*, 59(8):209–  
609 216, 2004. ISSN 0043-1656. doi: 10.1256/wea.73.04. URL [https://oceanrep.geomar.  
610 de/id/eprint/30311/](https://oceanrep.geomar.de/id/eprint/30311/). Number: 8 Publisher: Wiley-Blackwell.
- 611 P. Frich, L. V. Alexander, P. Della-Marta, B. Gleason, M. Haylock, A. M. G. K. Tank, and  
612 T. Peterson. Observed coherent changes in climatic extremes during the second half of the  
613 twentieth century. *Climate Research*, 19(3):193–212, Jan. 2002. ISSN 0936-577X, 1616-  
614 1572. doi: 10.3354/cr019193. URL [https://www.int-res.com/abstracts/cr/v19/n3/  
615 p193-212/](https://www.int-res.com/abstracts/cr/v19/n3/p193-212/).
- 616 M. Frihat, B. Podvin, L. Mathelin, Y. Fraigneau, and F. Yvon. Coherent structure identification  
617 in turbulent channel flow using Latent Dirichlet Allocation. *Journal of Fluid Mechanics*, 920:  
618 A27, Aug. 2021. ISSN 0022-1120, 1469-7645. doi: 10.1017/jfm.2021.444. URL [http:  
619 //arxiv.org/abs/2005.10010](http://arxiv.org/abs/2005.10010). arXiv: 2005.10010.
- 620 D. E. Hanley, M. A. Bourassa, J. J. O’Brien, S. R. Smith, and E. R. Spade. A Quan-  
621 titative Evaluation of ENSO Indices. *Journal of Climate*, 16(8):1249–1258, Apr. 2003.  
622 ISSN 0894-8755, 1520-0442. doi: 10.1175/1520-0442(2003)16<1249:AQEOEI>2.0.CO;2.

623 URL [https://journals.ametsoc.org/view/journals/clim/16/8/1520-0442\\_2003\\_](https://journals.ametsoc.org/view/journals/clim/16/8/1520-0442_2003_)  
624 [16\\_1249\\_aqeoie\\_2.0.co\\_2.xml](https://journals.ametsoc.org/view/journals/clim/16/8/1520-0442_2003_16_1249_aqeoie_2.0.co_2.xml). Publisher: American Meteorological Society Section:  
625 Journal of Climate.

626 H. Hersbach, B. Bell, P. Berrisford, S. Hirahara, A. Horányi, J. Muñoz-Sabater, J. Nicolas,  
627 C. Peubey, R. Radu, D. Schepers, A. Simmons, C. Soci, S. Abdalla, X. Abellan, G. Balsamo,  
628 P. Bechtold, G. Biavati, J. Bidlot, M. Bonavita, G. De Chiara, P. Dahlgren, D. Dee, M. Dia-  
629 mantakis, R. Dragani, J. Flemming, R. Forbes, M. Fuentes, A. Geer, L. Haimberger, S. Healy,  
630 R. J. Hogan, E. Hólm, M. Janisková, S. Keeley, P. Laloyaux, P. Lopez, C. Lupu, G. Radnoti,  
631 P. de Rosnay, I. Rozum, F. Vamborg, S. Villaume, and J.-N. Thépaut. The ERA5 global reanal-  
632 ysis. *Quarterly Journal of the Royal Meteorological Society*, 146(730):1999–2049, 2020. ISSN  
633 1477-870X. doi: 10.1002/qj.3803. URL [https://onlinelibrary.wiley.com/doi/abs/](https://onlinelibrary.wiley.com/doi/abs/10.1002/qj.3803)  
634 [10.1002/qj.3803](https://onlinelibrary.wiley.com/doi/abs/10.1002/qj.3803). eprint: <https://onlinelibrary.wiley.com/doi/pdf/10.1002/qj.3803>.

635 M. Hoffman, F. Bach, and D. Blei. Online Learning for Latent Dirichlet Allocation.  
636 In *Advances in Neural Information Processing Systems*, volume 23. Curran Associates,  
637 Inc., 2010. URL [https://proceedings.neurips.cc/paper\\_files/paper/2010/hash/](https://proceedings.neurips.cc/paper_files/paper/2010/hash/71f6278d140af599e06ad9bf1ba03cb0-Abstract.html)  
638 [71f6278d140af599e06ad9bf1ba03cb0-Abstract.html](https://proceedings.neurips.cc/paper_files/paper/2010/hash/71f6278d140af599e06ad9bf1ba03cb0-Abstract.html).

639 D. I. Jeong, B. Yu, and A. J. Cannon. Links between atmospheric blocking and North American  
640 winter cold spells in two generations of Canadian Earth System Model large ensembles. *Climate*  
641 *Dynamics*, 57(7):2217–2231, Oct. 2021. ISSN 1432-0894. doi: 10.1007/s00382-021-05801-0.  
642 URL <https://doi.org/10.1007/s00382-021-05801-0>.

643 V. V. Kharin, F. W. Zwiers, X. Zhang, and M. Wehner. Changes in temperature and precipitation ex-  
644 tremes in the CMIP5 ensemble. *Climatic Change*, 119(2):345–357, July 2013. ISSN 1573-1480.  
645 doi: 10.1007/s10584-013-0705-8. URL <https://doi.org/10.1007/s10584-013-0705-8>.

646 T. N. Krishnamurti. The subtropical jet stream of winter. *Journal of the Atmospheric Sciences*, 18  
647 (2):172–191, 1961.

648 C. Li, F. Zwiers, X. Zhang, G. Li, Y. Sun, and M. Wehner. Changes in Annual Extremes of  
649 Daily Temperature and Precipitation in CMIP6 Models. *Journal of Climate*, 34(9):3441–3460,  
650 May 2021. ISSN 0894-8755, 1520-0442. doi: 10.1175/JCLI-D-19-1013.1. URL <https://doi.org/10.1175/JCLI-D-19-1013.1>.



651 //journals.ametsoc.org/view/journals/clim/34/9/JCLI-D-19-1013.1.xml. Pub-  
652 lisher: American Meteorological Society Section: Journal of Climate.

653 Y. Liu, E. Racah, Prabhat, J. Correa, A. Khosrowshahi, D. Lavers, K. Kunkel, M. Wehner, and  
654 W. Collins. Application of Deep Convolutional Neural Networks for Detecting Extreme Weather  
655 in Climate Datasets. *arXiv:1605.01156 [cs]*, May 2016. URL <http://arxiv.org/abs/1605.01156>.  
656 arXiv: 1605.01156.

657 P. Lucas-Picher, D. Argüeso, E. Brisson, Y. Trambly, P. Berg, A. Lemonsu, S. Kotlarski, and  
658 C. Caillaud. Convection-permitting modeling with regional climate models: Latest develop-  
659 ments and next steps. *WIREs Climate Change*, 12(6):e731, 2021. ISSN 1757-7799. doi: 10.  
660 1002/wcc.731. URL <https://onlinelibrary.wiley.com/doi/abs/10.1002/wcc.731>.  
661 \_eprint: <https://onlinelibrary.wiley.com/doi/pdf/10.1002/wcc.731>.

662 A. R. Lupo. Atmospheric blocking events: A review. *Annals of the New York Academy of Sciences*,  
663 1504(1):5–24, 2021.

664 J. A. López-Bueno, M. Navas-Martín, J. Díaz, I. J. Mirón, M. Y. Luna, G. Sánchez-Martínez,  
665 D. Culqui, and C. Linares. The effect of cold waves on mortality in urban and rural areas  
666 of Madrid. *Environmental Sciences Europe*, 33(1):72, June 2021. ISSN 2190-4715. doi:  
667 10.1186/s12302-021-00512-z. URL <https://doi.org/10.1186/s12302-021-00512-z>.

668 M. McCarthy, N. Christidis, N. Dunstone, D. Fereday, G. Kay, A. Klein-Tank, J. Lowe,  
669 J. Petch, A. Scaife, and P. Stott. Drivers of the UK summer heatwave of  
670 2018. *Weather*, 74(11):390–396, 2019. ISSN 1477-8696. doi: 10.1002/wea.  
671 3628. URL <https://onlinelibrary.wiley.com/doi/abs/10.1002/wea.3628>. \_eprint:  
672 <https://onlinelibrary.wiley.com/doi/pdf/10.1002/wea.3628>.

673 G. A. Meehl, G. J. Boer, C. Covey, M. Latif, and R. J. Stouffer. The Coupled Model Intercomparison  
674 Project (CMIP). *Bulletin of the American Meteorological Society*, 81(2):313–318, Feb. 2000.  
675 ISSN 0003-0007, 1520-0477. doi: 10.1175/1520-0477(2000)081<0313:TCMIPC>2.3.CO;  
676 2. URL [http://journals.ametsoc.org/doi/10.1175/1520-0477\(2000\)081<0313:  
677 TCMIPC>2.3.CO;2](http://journals.ametsoc.org/doi/10.1175/1520-0477(2000)081<0313:TCMIPC>2.3.CO;2).

- 678 P.-A. Michelangeli, R. Vautard, and B. Legras. Weather Regimes: Recurrence and  
679 Quasi Stationarity. *Journal of the Atmospheric Sciences*, 52(8):1237–1256, Apr. 1995.  
680 ISSN 0022-4928, 1520-0469. doi: 10.1175/1520-0469(1995)052<1237:WRRMQS>2.0.CO;2.  
681 URL [https://journals.ametsoc.org/view/journals/atsc/52/8/1520-0469\\_1995\\_](https://journals.ametsoc.org/view/journals/atsc/52/8/1520-0469_1995_052_1237_wrraqs_2_0_co_2.xml)  
682 [052\\_1237\\_wrraqs\\_2\\_0\\_co\\_2.xml](https://journals.ametsoc.org/view/journals/atsc/52/8/1520-0469_1995_052_1237_wrraqs_2_0_co_2.xml). Publisher: American Meteorological Society Section:  
683 Journal of the Atmospheric Sciences.
- 684 J. Mignot, F. Hourdin, J. Deshayes, O. Boucher, G. Gastineau, I. Musat, M. Vancoppenolle,  
685 J. Servonnat, A. Caubel, F. Chéruy, S. Denvil, J.-L. Dufresne, C. Ethé, L. Fairhead, M.-  
686 A. Foujols, J.-Y. Grandpeix, G. Levavasseur, O. Marti, M. Menary, C. Rio, C. Rousset, and  
687 Y. Silvy. The Tuning Strategy of IPSL-CM6A-LR. *Journal of Advances in Modeling Earth*  
688 *Systems*, 13(5):e2020MS002340, 2021. ISSN 1942-2466. doi: 10.1029/2020MS002340.  
689 URL <https://onlinelibrary.wiley.com/doi/abs/10.1029/2020MS002340>. \_eprint:  
690 <https://onlinelibrary.wiley.com/doi/pdf/10.1029/2020MS002340>.
- 691 K. Papagiannaki, K. Lagouvardos, V. Kotroni, and G. Papagiannakis. Agricultural losses related to  
692 frost events: use of the 850 hPa level temperature as an explanatory variable of the damage cost.  
693 *Natural Hazards and Earth System Sciences*, 14(9):2375–2386, Sept. 2014. ISSN 1561-8633.  
694 doi: 10.5194/nhess-14-2375-2014. URL [https://nhess.copernicus.org/articles/14/](https://nhess.copernicus.org/articles/14/2375/2014/)  
695 [2375/2014/](https://nhess.copernicus.org/articles/14/2375/2014/). Publisher: Copernicus GmbH.
- 696 R. Řehůřek and P. Sojka. Software Framework for Topic Modelling with Large Corpora. In  
697 *Proceedings of the LREC 2010 Workshop on New Challenges for NLP Frameworks*, pages  
698 45–50, Valletta, Malta, May 2010. ELRA. <http://is.muni.cz/publication/884893/en>.
- 699 D. F. Rex. Blocking Action in the Middle Troposphere and its Effect upon Regional Climate.  
700 *Tellus*, 2(4):275–301, Jan. 1950. ISSN 0040-2826. doi: 10.3402/tellusa.v2i4.8603. URL  
701 <https://doi.org/10.3402/tellusa.v2i4.8603>. Publisher: Taylor & Francis \_eprint:  
702 <https://doi.org/10.3402/tellusa.v2i4.8603>.
- 703 D. Rodrigues, M. C. Alvarez-Castro, G. Messori, P. Yiou, Y. Robin, and D. Faranda. Dynamical  
704 Properties of the North Atlantic Atmospheric Circulation in the Past 150 Years in CMIP5 Models  
705 and the 20CRv2c Reanalysis. *Journal of Climate*, 31(15):6097–6111, Aug. 2018. ISSN 0894-  
706 8755, 1520-0442. doi: 10.1175/JCLI-D-17-0176.1. URL <https://journals.ametsoc>.

- 707 [org/view/journals/clim/31/15/jcli-d-17-0176.1.xml](https://journals.clim/31/15/jcli-d-17-0176.1.xml). Publisher: American Meteorological Society Section: Journal of Climate.
- 708
- 709 E. Rousi, K. Kornhuber, G. Beobide-Arsuaga, F. Luo, and D. Coumou. Accelerated western  
710 European heatwave trends linked to more-persistent double jets over Eurasia. *Nature Com-*  
711 *munications*, 13(1):3851, July 2022. ISSN 2041-1723. doi: 10.1038/s41467-022-31432-y.  
712 URL <https://www.nature.com/articles/s41467-022-31432-y>. Number: 1 Publisher:  
713 Nature Publishing Group.
- 714 A. A. Scaife, T. Woollings, J. Knight, G. Martin, and T. Hinton. Atmospheric Blocking and Mean  
715 Biases in Climate Models. *Journal of Climate*, 23(23):6143–6152, Dec. 2010. ISSN 0894-  
716 8755, 1520-0442. doi: 10.1175/2010JCLI3728.1. URL [https://journals.ametsoc.org/  
717 view/journals/clim/23/23/2010jcli3728.1.xml](https://journals.ametsoc.org/view/journals/clim/23/23/2010jcli3728.1.xml). Publisher: American Meteorological  
718 Society Section: Journal of Climate.
- 719 S. I. Seneviratne, X. Zhang, M. Adnan, W. Badi, C. Dereczynski, A. Di Luca, S. Ghosh, I. Iskandar,  
720 J. Kossin, S. Lewis, F. Otto, I. Pinto, M. Satoh, S. M. Vicente-Serrano, M. Wehner, and B. Zhou.  
721 Weather and climate extreme events in a changing climate. In V. Masson-Delmotte, P. Zhai,  
722 A. Pirani, S. L. Connors, C. Péan, S. Berger, N. Caud, Y. Chen, L. Goldfarb, M. I. Gomis,  
723 M. Huang, K. Leitzell, E. Lonnoy, J. B. R. Matthews, T. K. Maycock, T. Waterfield, Yelekçi,  
724 R. Yu, and B. Zhou, editors, *Climate Change 2021: The Physical Science Basis. Contribution  
725 of Working Group I to the Sixth Assessment Report of the Intergovernmental Panel on Climate  
726 Change*, pages 1513–1766. Cambridge University Press, Cambridge, United Kingdom and New  
727 York, NY, USA, 2021. doi: 10.1017/9781009157896.001.
- 728 N. C. Stenseth, G. Ottersen, J. W. Hurrell, A. Mysterud, M. Lima, K. Chan, N. G. Yoccoz,  
729 and B. Ådlandsvik. Studying climate effects on ecology through the use of climate indices:  
730 the North Atlantic Oscillation, El Niño Southern Oscillation and beyond. *Proceedings of the  
731 Royal Society of London. Series B: Biological Sciences*, 270(1529):2087–2096, Oct. 2003.  
732 doi: 10.1098/rspb.2003.2415. URL [https://royalsocietypublishing.org/doi/abs/  
733 10.1098/rspb.2003.2415](https://royalsocietypublishing.org/doi/abs/10.1098/rspb.2003.2415). Publisher: Royal Society.
- 734 N. C. Swart, J. N. S. Cole, V. V. Kharin, M. Lazare, J. F. Scinocca, N. P. Gillett, J. Anstey,  
735 V. Arora, J. R. Christian, S. Hanna, Y. Jiao, W. G. Lee, F. Majaess, O. A. Saenko, C. Seiler,

- 736 C. Seinen, A. Shao, M. Sigmond, L. Solheim, K. von Salzen, D. Yang, and B. Winter. The  
737 Canadian Earth System Model version 5 (CanESM5.0.3). *Geoscientific Model Development*, 12  
738 (11):4823–4873, Nov. 2019. ISSN 1991-959X. doi: 10.5194/gmd-12-4823-2019. URL <https://gmd.copernicus.org/articles/12/4823/2019/>. Publisher: Copernicus GmbH.
- 740 H. Tatebe, T. Ogura, T. Nitta, Y. Komuro, K. Ogochi, T. Takemura, K. Sudo, M. Sekiguchi, M. Abe,  
741 F. Saito, M. Chikira, S. Watanabe, M. Mori, N. Hirota, Y. Kawatani, T. Mochizuki, K. Yoshimura,  
742 K. Takata, R. O’ishi, D. Yamazaki, T. Suzuki, M. Kurogi, T. Kataoka, M. Watanabe, and  
743 M. Kimoto. Description and basic evaluation of simulated mean state, internal variability, and  
744 climate sensitivity in MIROC6. *Geoscientific Model Development*, 12(7):2727–2765, July 2019.  
745 ISSN 1991-959X. doi: 10.5194/gmd-12-2727-2019. URL <https://gmd.copernicus.org/articles/12/2727/2019/>. Publisher: Copernicus GmbH.
- 747 D. Valle, P. Albuquerque, Q. Zhao, A. Barberan, and R. J. Fletcher Jr. Extend-  
748 ing the Latent Dirichlet Allocation model to presence/absence data: A case study on  
749 North American breeding birds and biogeographical shifts expected from climate change.  
750 *Global Change Biology*, 24(11):5560–5572, 2018. ISSN 1365-2486. doi: 10.1111/  
751 gcb.14412. URL <https://onlinelibrary.wiley.com/doi/abs/10.1111/gcb.14412>.  
752 \_eprint: <https://onlinelibrary.wiley.com/doi/pdf/10.1111/gcb.14412>.
- 753 G. J. van Oldenborgh, S. Drijfhout, A. van Ulden, R. Haarsma, A. Sterl, C. Severijns, W. Hazeleger,  
754 and H. Dijkstra. Western Europe is warming much faster than expected. *Climate of the Past*,  
755 5(1):1–12, Jan. 2009. ISSN 1814-9324. doi: 10.5194/cp-5-1-2009. URL <https://cp.copernicus.org/articles/5/1/2009/>. Publisher: Copernicus GmbH.
- 757 R. Vautard. Multiple Weather Regimes over the North Atlantic: Analysis of Pre-  
758 cursors and Successors. *Monthly Weather Review*, 118(10):2056–2081, Oct. 1990.  
759 ISSN 1520-0493, 0027-0644. doi: 10.1175/1520-0493(1990)118<2056:MWROTN>2.0.CO;  
760 2. URL [https://journals.ametsoc.org/view/journals/mwre/118/10/1520-0493\\_1990\\_118\\_2056\\_mwrotn\\_2\\_0\\_co\\_2.xml](https://journals.ametsoc.org/view/journals/mwre/118/10/1520-0493_1990_118_2056_mwrotn_2_0_co_2.xml). Publisher: American Meteorological Society Sec-  
761 tion: Monthly Weather Review.
- 763 R. Vautard, J. Cattiaux, T. Happé, J. Singh, R. Bonnet, C. Cassou, D. Coumou, F. D’Andrea,  
764 D. Faranda, E. Fischer, A. Ribes, P. Yiou, and S. Sippel. Heat extremes in Western Europe are

765 increasing faster than simulated due to missed atmospheric circulation trends, Jan. 2023a. URL  
766 <https://hal.science/hal-03937057>.

767 R. Vautard, G. J. van Oldenborgh, R. Bonnet, S. Li, Y. Robin, S. Kew, S. Philip, J.-M. Soubeyrou,  
768 B. Dubuisson, N. Viovy, M. Reichstein, F. Otto, and I. Garcia de Cortazar-Atauri. Human  
769 influence on growing-period frosts like in early April 2021 in central France. *Natural Hazards  
770 and Earth System Sciences*, 23(3):1045–1058, Mar. 2023b. ISSN 1561-8633. doi: 10.5194/  
771 nhess-23-1045-2023. URL <https://nhess.copernicus.org/articles/23/1045/2023/>.  
772 Publisher: Copernicus GmbH.

773 J. M. Wallace and P. V. Hobbs. *Atmospheric science: an introductory survey*, volume 92. Elsevier,  
774 2006.

775 V. Weilhhammer, J. Schmid, I. Mittermeier, F. Schreiber, L. Jiang, V. Pastuhovic, C. Herr, and  
776 S. Heinze. Extreme weather events in europe and their health consequences – A systematic  
777 review. *International Journal of Hygiene and Environmental Health*, 233:113688, Apr. 2021.  
778 ISSN 1438-4639. doi: 10.1016/j.ijheh.2021.113688. URL [https://www.sciencedirect.  
779 com/science/article/pii/S1438463921000018](https://www.sciencedirect.com/science/article/pii/S1438463921000018).

780 T. Ziehn, M. A. Chamberlain, R. M. Law, A. Lenton, R. W. Bodman, M. Dix, L. Stevens, Y.-P. Wang,  
781 J. Srbinovsky, T. Ziehn, M. A. Chamberlain, R. M. Law, A. Lenton, R. W. Bodman, M. Dix,  
782 L. Stevens, Y.-P. Wang, and J. Srbinovsky. The Australian Earth System Model: ACCESS-  
783 ESM1.5. *Journal of Southern Hemisphere Earth Systems Science*, 70(1):193–214, Aug. 2020.  
784 ISSN 2206-5865, 2206-5865. doi: 10.1071/ES19035. URL [https://www.publish.csiro.  
785 au/es/ES19035](https://www.publish.csiro.au/es/ES19035). Publisher: CSIRO PUBLISHING.